

Deep imaging of absorption and scattering features by multispectral multiple scattering low coherence interferometry

YANG ZHAO,¹ JASON R. MAHER,¹ MOHAMED M. IBRAHIM,² JENNIFER S. CHIEN,² HOWARD LEVINSON,^{2,3} AND ADAM WAX^{1,*}

¹*Department of Biomedical Engineering, Duke University, Durham, NC 27708, USA*

²*Department of Surgery, Duke University Medical Center, Durham, NC 27708, USA*

³*Department of Pathology, Duke University Medical Center, Durham, NC 27708, USA*

**a.wax@duke.edu*

Abstract: We have developed frequency domain multispectral multiple scattering low coherence interferometry (ms2/LCI) for deep imaging of absorption and scattering contrast. Using tissue-mimicking phantoms that match the full scattering phase function of human dermal tissue, we demonstrate that ms2/LCI can provide a signal/noise ratio (SNR) improvement of 15.4 dB over conventional OCT at an imaging depth of 1 mm. The enhanced SNR and penetration depth provided by ms2/LCI could be leveraged for a variety of clinical applications including the assessment of burn injuries where current clinical classification of severity only provides limited accuracy. The utility of the approach was demonstrated by imaging a tissue phantom simulating a partial-thickness burn revealing good spectroscopic contrast between healthy and injured tissue regions deep below the sample surface. Finally, healthy rat skin was imaged *in vivo* with both a commercial OCT instrument and our custom ms2/LCI system. The results demonstrate that ms2/LCI is capable of obtaining spectroscopic information far beyond the penetration depth provided by conventional OCT.

©2016 Optical Society of America

OCIS codes: (170.6510) Spectroscopy, tissue diagnostics; (290.4210) Multiple scattering; (110.1650) Coherence imaging.

References and links

1. A. Wax and J. E. Thomas, "Measurement of smoothed Wigner phase-space distributions for small-angle scattering in a turbid medium," *J. Opt. Soc. Am. A* **15**(7), 1896–1908 (1998).
2. M. G. Giacomelli and A. Wax, "Imaging beyond the ballistic limit in coherence imaging using multiply scattered light," *Opt. Express* **19**(5), 4268–4279 (2011).
3. T. E. Matthews, M. G. Giacomelli, W. J. Brown, and A. Wax, "Fourier domain multispectral multiple scattering low coherence interferometry," *Appl. Opt.* **52**(34), 8220–8228 (2013).
4. A. D. Jaskille, J. W. Shupp, M. H. Jordan, and J. C. Jeng, "Critical review of burn depth assessment techniques: Part I. Historical review," *J. Burn Care Res.* **30**(6), 937–947 (2009).
5. *American National Standard for the Safe Use of Lasers Z136. 1–2007*. Laser Institute of America, Orlando, FL., 2007.
6. T. E. Matthews, M. Medina, J. R. Maher, H. Levinson, W. J. Brown, and A. Wax, "Deep tissue imaging using spectroscopic analysis of multiply scattered light," *Optica* **1**(2), 105–111 (2014).
7. F. Robles, R. N. Graf, and A. Wax, "Dual window method for processing spectroscopic optical coherence tomography signals with simultaneously high spectral and temporal resolution," *Opt. Express* **17**(8), 6799–6812 (2009).
8. E. E. Di Iorio, "Preparation of derivatives of ferrous and ferric hemoglobin," *Methods Enzymol.* **76**, 57–72 (1981).
9. K. Dalziel and J. R. O'Brien, "Side reactions in the deoxygenation of dilute oxyhaemoglobin solutions by sodium dithionite," *Biochem. J.* **67**(1), 119–124 (1957).
10. K. Hamada, T. Okazaki, R. Shukuya, and K. Kaziro, "The deoxygenation of dilute oxyhemoglobin by sodium dithionite," *J. Biochem.* **52**, 374–376 (1962).
11. F. Bevilacqua and C. Depeursinge, "Monte Carlo study of diffuse reflectance at source-detector separations close to one transport mean free path," *J. Opt. Soc. Am. A.* **16**(12), 2935–2945 (1999).
12. S. C. Kanick, D. M. McClatchy 3rd, V. Krishnaswamy, J. T. Elliott, K. D. Paulsen, and B. W. Pogue, "Sub-diffusive scattering parameter maps recovered using wide-field high-frequency structured light imaging," *Biomed. Opt. Express* **5**(10), 3376–3390 (2014).

13. S. L. Jacques, "Optical properties of biological tissues: a review," *Phys. Med. Biol.* **58**(11), R37–R61 (2013).
14. A. N. Bashkatov, E. A. Genina, and V. V. Tuchin, "Optical properties of skin, subcutaneous, and muscle tissues: a review," *J. Innov. Opt. Health Sci.* **04**(01), 9–38 (2011).
15. R. Graaff, A. C. Dassel, M. H. Koelink, F. F. de Mul, J. G. Aarnoudse, and W. G. Zijlstra, "Optical properties of human dermis in vitro and in vivo," *Appl. Opt.* **32**(4), 435–447 (1993).
16. D. Passos, J. C. Hebden, P. N. Pinto, and R. Guerra, "Tissue phantom for optical diagnostics based on a suspension of microspheres with a fractal size distribution," *J. Biomed. Opt.* **10**(6), 064036 (2005).
17. B. Gélébart, E. Tinet, J. M. Tualle, and S. Avriplier, "Phase function simulation in tissue phantoms: a fractal approach," *J. Eur. Opt. Soc. Part A* **5**(4), 377–388 (1996).
18. S. L. Jacques, C. A. Alter, and S. A. Prahl, "Angular dependence of HeNe laser light scattering by human dermis," *Lasers in the Life Sciences* **2**(4), 309–333 (1988).
19. J. R. Maher, V. Jaedicke, M. Medina, H. Levinson, M. A. Selim, W. J. Brown, and A. Wax, "In vivo analysis of burns in a mouse model using spectroscopic optical coherence tomography," *Opt. Lett.* **39**(19), 5594–5597 (2014).
20. Y. Zhao, J. R. Maher, J. Kim, M. A. Selim, H. Levinson, and A. Wax, "Evaluation of burn severity in vivo in a mouse model using spectroscopic optical coherence tomography," *Biomed. Opt. Express* **6**(9), 3339–3345 (2015).
21. A. M. Smith, M. C. Mancini, and S. Nie, "Bioimaging: second window for in vivo imaging," *Nat. Nanotechnol.* **4**(11), 710–711 (2009).

1. Introduction

Light scattering limits the penetration depth of optical imaging by attenuating the ballistic signal and obscuring it with a diffuse background. Techniques to separate the ballistic signal from the diffuse background include confocal microscopy and optical coherence tomography (OCT). Confocal microscopy employs a spatial gate (a confocal pinhole) while OCT uses a coherence gate to reject multiply scattered photons. However, forward-scattered light carries structural information about the tissue even after multiple scattering events [1] and it is therefore potentially feasible to utilize this light for deep imaging into tissue well beyond the ballistic limit [2].

Our recently developed frequency domain multispectral multiple scattering low coherence interferometry (ms2/LCI) technique enables depth-resolved, spectroscopic imaging at extended depth. It combines coherence gating with off-axis illumination and detection, enabling imaging of multiply forward-scattered photons through nearly 90 mean free scattering paths [3]. In this article, we demonstrate the detection of biologically relevant absorption and scattering features with ms2/LCI. The instrument is used to image a variety of samples including hemolyzed blood with various oxygenation levels and polystyrene microspheres of multiple sizes. We also designed and fabricated tissue-mimicking phantoms that match the full scattering phase function of human dermal tissue. Using these tissue phantoms, we found that our ms2/LCI instrument provides a signal-to-noise ratio (SNR) improvement of greater than 15 dB over conventional OCT at an imaging depth of 1 mm. Enhanced SNR and penetration depth may be beneficial for clinical applications such as the assessment of partial thickness burns that generally extend a few millimeters below the skin surface and are currently assessed by subjective visual inspections that provide limited accuracy [4]. Finally, the instrument was applied to acquire spectroscopic images of a partial-thickness burn tissue phantom and normal rat skin *in vivo* at depths exceeding those generally available in conventional LCI and OCT.

2. Instrumentation

A schematic diagram of the ms2/LCI system is shown in Fig. 1. The light source is a supercontinuum laser source (Fianium SC-450-4) with its output filtered using a near infrared (NIR) bandpass filter (809/81 nm Brightline bandpass filter, Semrock, Rochester, NY) to obtain a spectral range of 770–840 nm. The NIR optical window was chosen to provide increased penetration depth in tissue. A Mach-Zehnder configuration comprised of two 90:10 beamsplitter cubes was used to generate the interference signal between the sample and reference arms. This signal was coupled into a 5- μm -core, single mode fiber and delivered to a custom spectrometer with 52 pm spectral resolution [3]. The power delivered to the sample

plane was adjusted with a variable neutral density filter and was set at approximately 19 mW, which is below the maximum permissible exposure limit for skin set by the American National Standards Institute [5]. The spot size on the sample was measured to be 29 μm . Both the illumination and detection arms were placed on translation stages allowing for precise control of both the illumination and detection angle. The maximum illumination/detection angle allowed with this configuration is 6° , which is limited by the numerical aperture of lens L1 (NA = 0.13). Depth-resolved spectroscopic data were extracted from the detected interferograms using a Short-time Fourier transform (STFT) or the Dual Window (DW) method [6, 7].

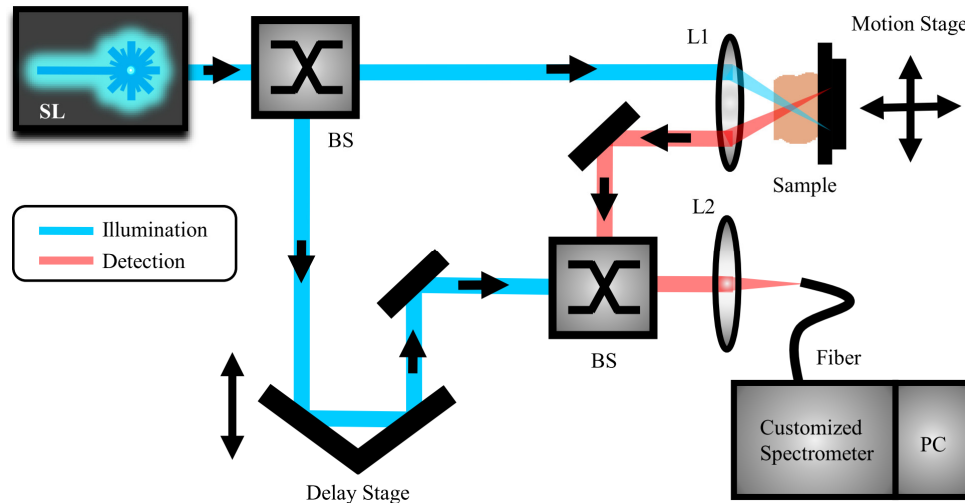


Fig. 1. Schematic plot of the ms2/LCI system. (SL – Supercontinuum Fiber Laser; BS – Beam Splitter; L – Lens).

The SNR of the system was determined by placing a mirror in the sample plane and calculating the ratio of the amplitude of the peak signal to the standard deviation of the noise. Figure 2 shows the SNR versus pathlength mismatch between sample and reference arms and also versus total acquisition time in seconds. Note that the SNR is lower than previously reported [3] due to the lower quantum efficiency of the CCD camera in the NIR (previous studies were performed in the visible range) as well as a shorter integration time.

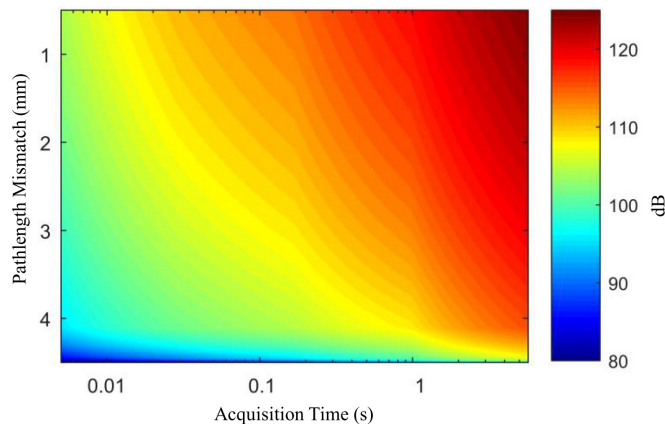


Fig. 2. Experimental measurements of SNR of the ms2/LCI system versus pathlength mismatch and acquisition time.

3. Feasibility studies

3.1 Absorption contrast

The feasibility of detecting absorption features in this spectral range (770-840nm) with the ms2/LCI system was examined by measuring the oxygen saturation level or oxygenation (SO_2) of hemolyzed blood samples. Whole blood from healthy volunteers was centrifuged to separate erythrocytes from other components. The erythrocytes were then hemolyzed and diluted with water to produce a hemoglobin concentration of approximately 80 g/L. Hemoglobin (Hb) is a protein molecule that has a high affinity for oxygen (often denoted as HbO_2 after binding with oxygen molecule), which means that hemolyzed blood exposed to air typically has an SO_2 value close to 100% [8, 9]. Different SO_2 levels were created by adding varying concentrations of sodium dithionite ($Na_2S_2O_4$), a deoxygenation agent, to the hemolyzed blood samples ($N = 11$ total) [10].

Each hemolyzed blood sample was drawn into a capillary tube (300 μm thickness, #3530-050, VitroCom, Mountain Lakes, NJ) and absorption spectra were measured using both a commercial UV-VIS spectrophotometer (UV-1800, Shimadzu Scientific, Kyoto, Japan) and the ms2/LCI instrument. During the ms2/LCI measurements, a mirror reflector was placed below the cuvette to measure light transmission through the sample. Both measurements were analyzed with a customized algorithm written in Matlab (R2015a, Mathworks, Natick, MA) to calculate the concentrations of Hb and HbO_2 , as well as SO_2 .

The attenuation $A(\lambda)$ of a sample in the single-scattering regime is related to its transmittance $T(\lambda)$ by the Beer-Lambert Law

$$A(\lambda) = -\log(T(\lambda)) = -\log\left(\frac{I(\lambda)}{I_0(\lambda)}\right) = -\log(e^{-\mu_{att}(\lambda)L}) \quad (1)$$

where $\mu_{att}(\lambda)$ is the attenuation coefficient of the sample and L is the path length. The attenuation coefficient of each hemolyzed blood sample is given by

$$\mu_{att}(\lambda) = \ln(10) \cdot [(\epsilon_{HbO_2}(\lambda) \cdot c_{HbO_2}) + (\epsilon_{Hb}(\lambda) \cdot c_{Hb}) + \mu_s(\lambda)] \quad (2)$$

where $\epsilon(\lambda)$ and c are the extinction coefficients and concentrations of oxy- and deoxy-hemoglobin and $\mu_s(\lambda)$ is the scattering coefficient. Attenuation in the sample is due to the combined absorbance of both Hb and HbO_2 as well as a scattering component $\mu_s(\lambda)$ that can be fitted with a power-law curve ($\mu_s(\lambda) = A\lambda^{-b}$). This scattering component may result from blood residues that are not fully removed during the hemolyzation procedures.

The attenuation coefficient of each hemolyzed blood sample was measured separately with the ms2/LCI system and spectrophotometer and each data set was fit with four parameters (c_{HbO_2} , c_{Hb} , A and b) by minimizing the root-mean square error (RMSE) between the fit and the measured data. The SO_2 level extracted with the ms2/LCI system was then compared with the corresponding, gold-standard spectrophotometer measurement.

Figure 3(a)-3(b) shows representative fits of spectra from a single hemolyzed blood sample. The SO_2 calculated with ms2/LCI (59%) was in good agreement with the gold-standard value determined with the spectrophotometer (52%). In Fig. 3(c), the ms2/LCI SO_2 measurements of all 11 samples are plotted against the corresponding spectrophotometer measurements. A small positive bias can be observed; however, the measurements are highly correlated ($r^2 = 0.961$, $p < 0.01$) with the gold-standard spectrophotometer data.

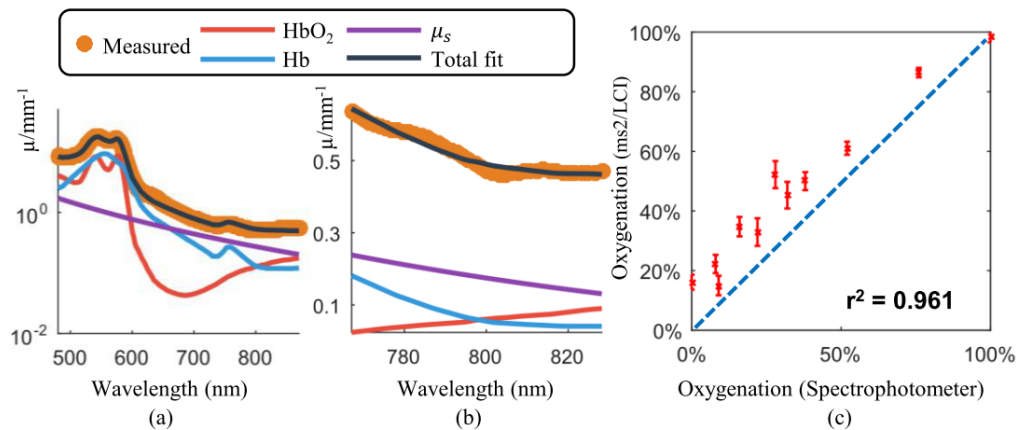


Fig. 3. Representative spectra acquired with (a) the spectrophotometer and (b) the ms2/LCI system. The SO_2 determined with ms2/LCI is in good agreement with the gold standard spectrophotometer measurement. (c) The ms2/LCI - derived SO_2 values from the full sample set are highly correlated ($r^2 = 0.961$, $p < 0.01$) with the gold standard spectrophotometer measurements (Error bars: 95% confidence interval).

3.2 Scattering contrast

Scattering plays a fundamental role in light-tissue interaction and is the dominant mechanism in light transport processes [6]. To demonstrate the feasibility of measuring scattering features with ms2/LCI, scattering phantoms were fabricated with polystyrene microspheres (Thermo Scientific 3000, Duke Scientific, Microgenics Corporation, Fremont, CA). Two types of microspheres, with mean diameters of 4 μm (1.0% variance) and 10 μm (0.9% variance) were dried from suspension onto the surface of glass coverslips ($L \approx 200 \mu\text{m}$). The collection numerical aperture of the ms2/LCI scheme is calculated to be only 0.015 and the variation in Mie spectra across this small collection aperture is not significant. Thus computational complexity was reduced by approximating light collection only from a single angle. The wavelength-dependent backscattering from the spheres was measured by processing raw spectral data with the DW method. These backscattered spectra were then compared to a library of scattering spectra built with Mie theory. The library contained theoretical scattering spectra from microspheres with diameters ranging from 1 to 15 μm with distribution standard deviations of 0%, 0.2%, 0.4%, 0.6%, 0.8% and 1.0% of the mean diameter. The best fit was determined by computing $1/\chi^2$ values for each theoretical spectrum and finding the maximum value.

Figure 4(a) shows the $1/\chi^2$ values between the ms2/LCI measured data and theoretical spectra calculated using Mie theory. The best fits for the 4 and 10 μm microspheres were found to be 4.21 μm (distribution standard deviation of 0%) and 10.00 μm (distribution standard deviation of 0.4%) respectively. Size estimates derived from the ms2/LCI data of both sphere sizes closely match the manufacturer-provided specifications. The measured data and best fit for the two sphere sizes are illustrated in Fig. 4(b)-4(c).

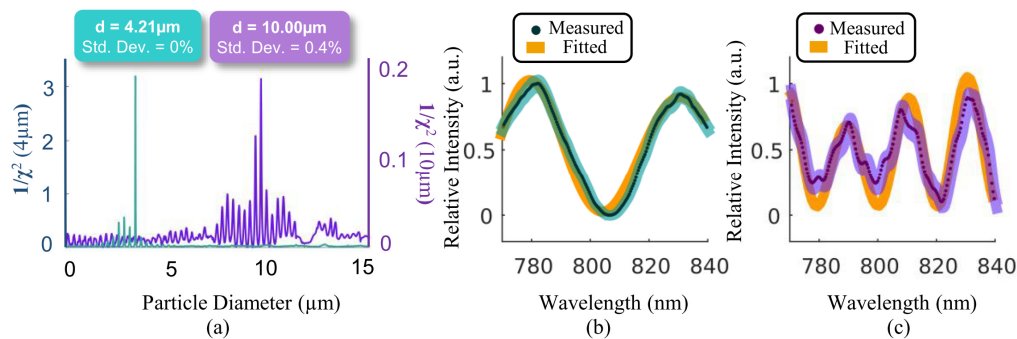


Fig. 4. (a) Size estimation of 4 μm and 10 μm microspheres by $1/\chi^2$ maximization. ms2/LCI - measured data of (b) $d = 4\mu\text{m}$ and (c) $d = 10\mu\text{m}$ microspheres with their best fits ($d = 4.21\mu\text{m}$ and $d = 10.00\mu\text{m}$ respectively; shaded area represents the 95% confidence interval of measurements; data were normalized to unit intensity and zero background prior to fitting).

4. Tissue phantom design and imaging results

Many tissue phantoms aim to match both the scattering coefficient (μ_s) and anisotropy (g) of a selected target tissue. However, it may not be sufficient to match those parameters alone as they do not fully reflect the angular distribution of light scattered by the tissue [11, 12]. For example, the scattering anisotropy (or average cosine of the scattering angle) of human skin generally ranges from 0.7 to 0.85 [13–15]. In the NIR, phantoms with scattering anisotropy in this range can be fabricated with polystyrene microspheres with diameters between 0.4 and 0.7 μm embedded in a polydimethylsiloxane (PDMS) matrix. Although this approach matches the scattering anisotropy of tissue, it does not fully match the scattering phase function.

In an effort to better model light transport in skin, we aimed to create phantoms that better matched the scattering phase function. In this study, all tissue phantoms were fabricated by mixing polystyrene microspheres (Thermo Scientific 3000, Duke Scientific, Microgenics Corporation, Fremont, CA) into a polydimethylsiloxane (PDMS) base agent (Dow Corning, Midland, MI). The solution was stirred and mixed with a curing agent at a 10:1 base-to-curing-agent ratio. Air bubbles were removed by placing the mixture in a vacuum chamber for one hour and the phantoms were cured at 60°C for 6 hours.

4.1 Matching the full scattering phase function of biological tissue

One approach used to match the phase function of skin is to utilize polydisperse microspheres, i.e., a suspension of microspheres with various sizes. Previous studies have demonstrated the feasibility of matching tissue phase functions using polydisperse microspheres with a fractal size distribution [16, 17]. Here, we chose to use microspheres with three different diameters ($d = 0.102\mu\text{m}$, 1.6 μm , 10 μm). The theoretical angular scattering profile was calculated for each size microsphere and these profiles were fit to a reference scattering phase function for human dermal tissue [18]. The result of the fit, including the volume percent of each sphere required to match the full scattering phase function, is shown in Table 1 and Fig. 5(a) below. This distribution of sphere sizes provides a scattering anisotropy matching healthy human dermis ($g = 0.78$) and closely matches the full scattering phase function. The concentration of the microsphere suspension was also controlled to provide a scattering coefficient $\mu_s = 9.1\text{ mm}^{-1}$ and therefore a reduced scattering coefficient $\mu_s' = \mu_s(1-g) \approx 2\text{ mm}^{-1}$, which closely matches skin [13].

Table 1. Composition of polydisperse phantom (healthy tissue). d is the diameter of the microspheres and $v/v\%$ is the volume relative to the total volume of the spheres.

Polydisperse Phantom (Healthy Tissue)			
d (μm)	0.102	1.6	10
$v/v\%$	91.62%	4.69%	3.69%

Figure 5(a) shows the simulated phase functions of healthy human dermis compared to both the scattering phantoms fabricated with multiple sphere sizes (polydisperse, $d = 0.102\ \mu\text{m}$, $1.6\ \mu\text{m}$, $10\ \mu\text{m}$), and those with a single sphere size (monodisperse, $d = 0.56\ \mu\text{m}$). Both phantoms were designed to match the anisotropy ($g = 0.78$) and scattering coefficient ($\mu_s = 9.1\ \text{mm}^{-1}$) of dermal tissue, but only the polydisperse phantom provided a good match across the full scattering phase function.

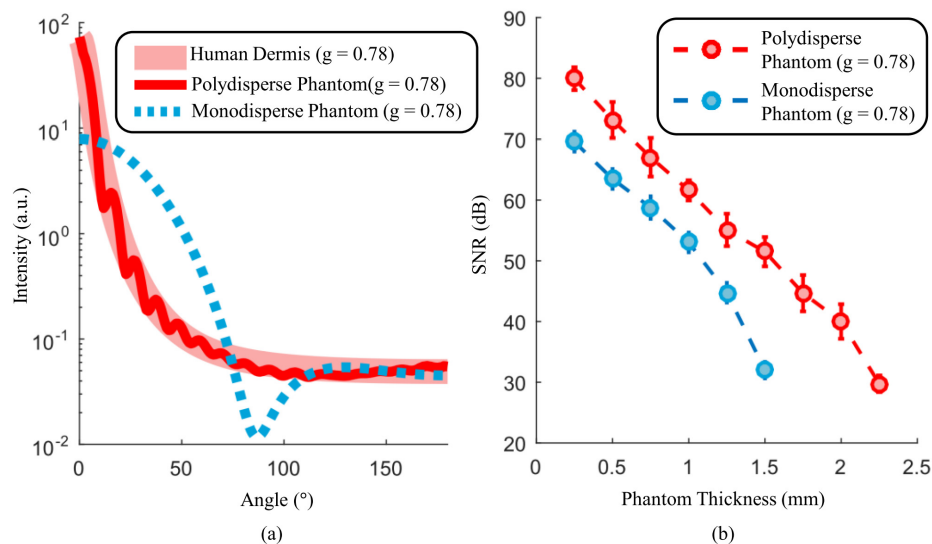


Fig. 5. (a) Phase functions of human dermis and scattering phantoms fabricated with multiple sphere sizes (polydisperse, $d = 0.102\ \mu\text{m}$, $1.6\ \mu\text{m}$, $10\ \mu\text{m}$) and a single sphere size (monodisperse, $d = 0.56\ \mu\text{m}$). (b) SNR of mirror reflector imaged beneath phantoms of various thickness. (Error bars: 95% confidence interval).

To further explore differences between the phantoms, a mirror reflector was imaged beneath varying thicknesses of each sample. The SNR falloff as a function of tissue phantom thickness is plotted in Fig. 5(b). The figure shows an SNR difference of more than 20 dB at a depth of 1.5 mm. This difference suggests that the full scattering phase function must be matched to provide an accurate assessment of photon migration and overall instrument performance. Based on these results, we chose to match the full scattering phase function in all subsequent tissue phantoms, rather than matching μ_s and g alone.

4.2 Comparison of tissue phantom imaging with ms2/LCI and conventional LCI

The SNR advantage of off-axis illumination/detection has been qualitatively discussed in earlier studies by our group [2, 3, 6]. Here, we provide a quantitative assessment of system performance as a function of illumination/detection angle (α). We examined changes in system SNR over different illumination/detection angles by measuring a reflector under a 1-mm, skin-mimicking tissue phantom. The illumination/detection angles were precisely controlled by translating the illumination and detection apertures relative to the final objective lens in the sample arm. The results of this experiment are plotted in Fig. 6 showing that

ms2/LCI can provide an SNR improvement of 15.4 dB over conventional LCI ($\alpha = 0^\circ$) by utilizing an offset angle of $\alpha = 3^\circ$. This could be caused by smaller angles ($\alpha < 3^\circ$) rejecting less out-of-focus light (i.e., there is a larger overlap of the illumination and collection regions) while larger angles ($\alpha > 3^\circ$) yield longer photon path lengths in the tissue causing increased attenuation. The illumination/detection angles were the only variables that were changed during these experiments, which all used the same scattering phantom. Therefore, this 15.4 dB gain is achieved solely by moving from on-axis to off-axis illumination/detection regime.

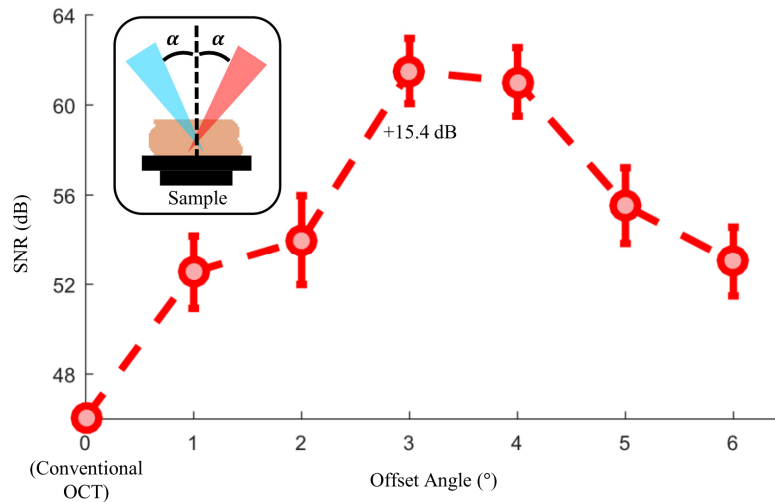


Fig. 6. SNR of mirror reflector under 1 mm of polydisperse tissue phantom. The SNR value at 0 offset angle corresponds to a conventional LCI setup. A maximum SNR gain of 15.4 dB is achieved at an offset angle of $\alpha = 3^\circ$. (Error bars: 95% confidence interval; inset: a schematic plot of the illumination/detection path).

4.3 Tissue phantom of burned skin

We have demonstrated that polydisperse microspheres can be used to create tissue phantoms that mimic the optical properties of healthy skin. Here, we present a tissue phantom for burned skin to illustrate the feasibility of detecting burn injuries with ms2/LCI. Like the healthy tissue phantom, the burned phantom was fabricated using three sizes of polydisperse microspheres; however, the volume percentages, shown in Table 2, were adjusted to yield a scattering spectrum that matched that of previous measurements of burned tissue [19, 20].

Table 2. Composition of polydisperse phantom (burned tissue). d is the diameter of the microspheres and $v/v\%$ is the volume relative to the total volume of the spheres.

Polydisperse Phantom (Burned Tissue)			
d (μm)	0.102	1.6	10
$v/v\%$	56.22%	33.35%	10.43%

Two-layer samples consisting of burned and healthy tissue phantoms were constructed and imaged with ms2/LCI. The extracted spectrum associated with each pixel was fitted with a power-law model of the form of $A\lambda^{-b}$ where λ is wavelength and A , b are fitted parameters. Representative spectra of both healthy and burned tissue layers along with their corresponding power-law fits are shown in Fig. 7(a). The power-law exponents of both the burned and healthy phantom ($b = -1.3$ and 1.2 , respectively) are similar to those reported in earlier studies [19, 20], which showed $b = -1.4$ and 1.8 for burned and healthy tissue when fit across the same bandwidth (770-830 nm) used in this study. Figure 7(b) shows color coded

images of layered phantoms in which each pixel in the full cross-sectional image was color coded based on the power-law exponent. The color map is designed so that dark red color represents a small power-law exponent, which suggests burned tissue; while a light pink color represents a large power-law exponent suggesting healthy tissue. These images show good spectroscopic contrast between burned and healthy tissue regions and more importantly, they revealed an improved penetration depth of approximately 750 μm , which is much higher than the previously reported depth of $\sim 250 \mu\text{m}$ for conventional OCT measurements [19, 20].

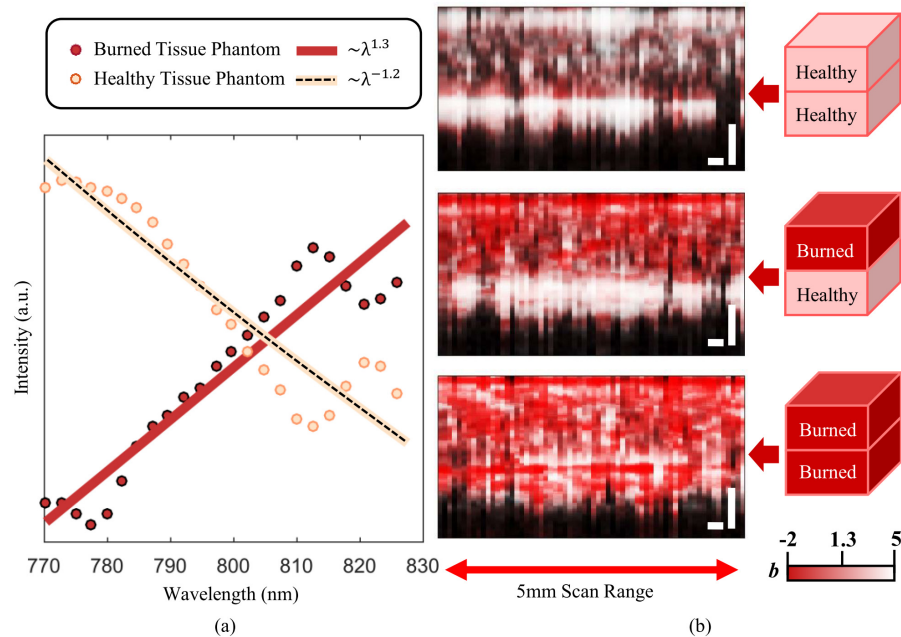


Fig. 7. (a) Spectra of burned and healthy tissue phantoms measured by ms2/LCI and their corresponding power-law fits. (b) Color coded images of layered phantoms using power-law exponent reveal differences between burned and healthy tissue with a larger lateral scan range and an improved penetration depths compared to [20] (Arrow pointing to tissue phantom interface, scale bars: 250 μm).

5. In vivo rat skin imaging

All animal procedures were performed in accordance with a protocol approved by the Institutional Animal Care and Use Committee (IACUC) at Duke University. Male Sprague-Dawley type rats ($N = 3$), weighing 250-300 grams (Charles River Laboratories, Wilmington, MA) were used throughout the study. The rats were housed under protocols approved by the Duke University IACUC.

Prior to imaging, rats were anesthetized using gas anesthesia (oxygen, 2 L/min, isoflurane, 2%). The dorsum was shaved and imaged with both a commercial, spectral-domain OCT system (Spark DRC, Wasatch Photonics Inc., Durham, NC) and the ms2/LCI system. The commercial OCT system possesses a center wavelength of 850 nm and bandwidth of 155 nm and a spot size of 29 μm on sample. The data acquired with this system were cropped to the 770-840 nm spectral range to match the bandwidth of the ms2/LCI system. During the ms2/LCI measurements, the optical focus is positioned at $\sim 1.25 \text{ mm}$ below the skin surface. Because of the natural curvature of the rat dorsum, we chose to scan a relatively small, but locally-flat, field-of-view of approximately 0.4 mm to construct each ms2/LCI and OCT image. This allowed the optical focus to remain at a fixed depth relative to the skin surface. The integration time of our CCD is approximately 5.3ms and 16 spectra were averaged for

each A-scan measurement. The camera speed was much faster compared to our previous work [6] so as to reduce the effect of blurring caused by the respiration movement of rat during the acquisition period. The increase in imaging speed is achieved at the expense of a lower SNR, which results in a reduced penetration depth in these measurements compared to previous ones with this instrument. Representative images of rat skin acquired with the OCT and ms2/LCI systems are shown in Fig. 8(a)-8(b). The epidermis and dermis of rat skin is clearly observed and labeled (E-epidermis, D-dermis) in the OCT image. The ms2/LCI image shows periodic structures across lateral positions which are caused by respirational movement during the 150 second imaging period. Although not as pronounced as the OCT image, the dermal-epidermal junction can still be distinguished. These images qualitatively show the improved penetration depth provided by ms2/LCI.

Raw spectra acquired with both the OCT and the ms2/LCI system were processed using a STFT and the depth resolved spectra were fitted with the same power-law model described in Section 4.3. Figure 8(c) shows representative depth-dependent tissue spectra acquired with OCT and ms2/LCI. Similar power-law exponents b were extracted from the OCT and ms2/LCI data at depths up to 300 μm , which is the maximum practical penetration depth provided by the commercial OCT system. The ms2/LCI system is able to image significantly deeper to a maximum practical depth of approximately 750 μm . This advantage in penetration depth is explicitly shown in Fig. 8(d) where the power-law exponents extracted with OCT and ms2/LCI are plotted versus depth.

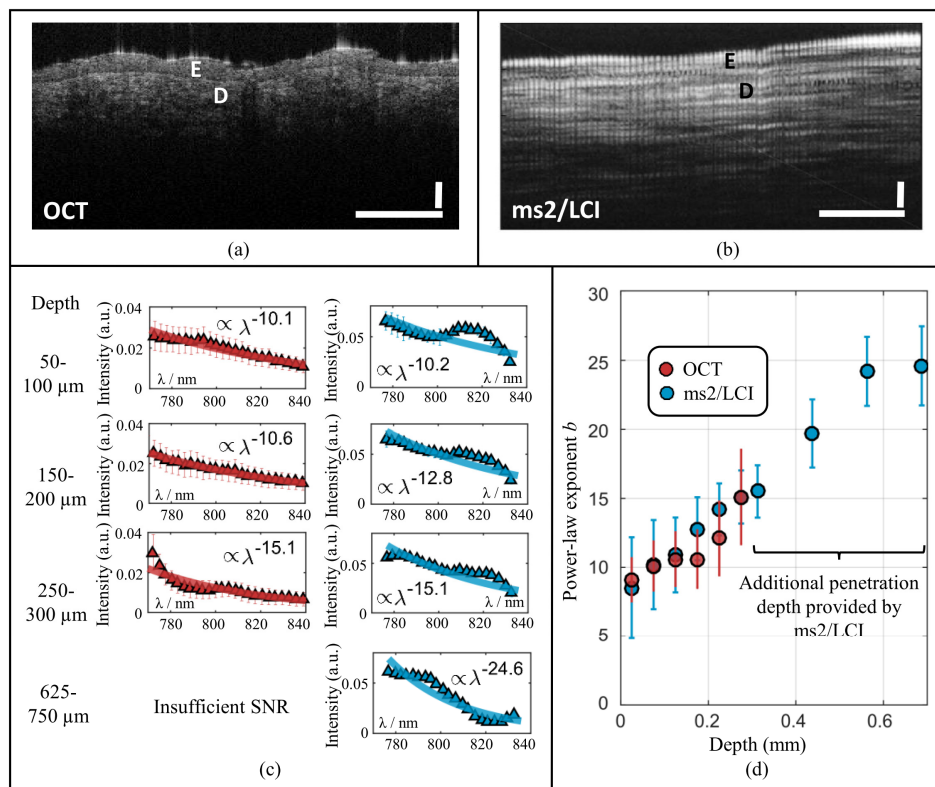


Fig. 8. (a) OCT and (b) ms2/LCI image of rat skin, ms2/LCI image reveals deeper tissue structures which is not observable in OCT image. Periodic structures across lateral positions are caused by respirational movement during imaging period. (E-epidermis, D-dermis, scale bars: 100 μm) (c) Representative depth-dependent tissue spectra calculated from OCT and ms2/LCI acquired data. (d) Power-law exponent b of OCT and ms2/LCI acquired spectra at different depths. Similar b values are found between OCT and ms2/LCI acquired spectra at the same depth. (Error bars: 95% confidence interval).

6. Conclusion

In summary, we have demonstrated deep spectroscopic tissue imaging with ms2/LCI. A controlled study was conducted demonstrating the superior penetration ability of off-axis configuration over on-axis configuration in this interferometric setup. A 15.6dB improvement in SNR at an imaging depth of 1 mm is observed using a tissue-phantom that matched the full scattering phase function of human dermal tissue. A variety of samples and tissue phantoms were examined here to characterize the sensitivity of the instrument to relevant biological absorption and scattering features. In addition, the instrument was also applied to measure rat skin *in vivo* and the results were compared to conventional OCT. A direct comparison between the depth-dependent spectra acquired by both systems was presented and results show that they share the same spectroscopic trends.

As aforementioned, the ms2/LCI system was operated in the NIR wavelength range to provide improved penetration depth in tissue [21]. Scattering is the dominant process in tissue in this wavelength range and most biological absorption features are therefore overwhelmed by the scattered signal. The effects of scattering can be observed in the hemolyzed blood samples [Fig. 3(b)] where scattering complicates the extraction of accurate blood oxygenation values. Because the scattering coefficient of skin is even larger than that of hemolyzed blood, the detection of tissue hemoglobin absorption with our system is likely not feasible in this wavelength range.

Although the depth-resolved tissue spectra are modeled well by a power-law, we observed other spectral features that are not fully described by this model [cf. Fig. 8(c)]. The interpretation of these features is the subject of ongoing study, which may benefit from more detailed comprehensive modeling of tissue scatterers and light transport. Furthermore, in order to extract the scattering coefficients from these depth-dependent spectra, precise knowledge of the optical path length is needed. However, this can be difficult to determine for multiply scattered photons and will be the subject of future studies. In spite of this shortcoming, a clear agreement in the spectroscopic trends of both the OCT and ms2/LCI data were seen up to the penetration limit of the OCT system. This study also experimentally demonstrated that the ms2/LCI system achieves more than twice the penetration depth of the commercial OCT system, both of which are operating in the same wavelength range. Overall, these results support the feasibility of utilizing ms2/LCI for deep spectroscopic imaging of skin disease or injury.

Funding

National Institutes of Health (NIH) (R01 HD072702, P30AR066527).